Available Online: 19 May 2026 DOI: 10.54254/2977-3903/2026.33644

Coherent Ising machine based on heterogeneous photonics integrated circuit for solving currency arbitrage problem

Changxin Zheng*, Yuanye Xing, Ziyao Zhang, Guanyu Chen

Key Laboratory of Optoelectronic Technology & Systems (Ministry of Education) and College of Optoelectronic Engineering, Chongqing University, Chongqing, China

*Corresponding Author. Email: gychen@cqu.edu.cn

Abstract. Coherent Ising machines (CIMs) have emerged as a compelling hardware paradigm for accelerating the solution of complex combinatorial optimization problems. In this work, we demonstrate an opto-electronic CIM architecture implemented on a heterogeneous photonic integrated circuit (PIC) platform. Our design monolithically integrates silicon nitride (SiN) waveguides, for ultra-low optical loss, with lithium niobate (LN) for high-speed Mach-Zehnder modulation, alongside integrated germanium-silicon (Ge-Si) photodetectors (PDs). By leveraging the strong Pockels effect of the SiN-LN hybrid platform, we exploit the intrinsic nonlinear transfer function of the modulator to emulate Ising spin dynamics within an opto-electronic feedback loop, thereby bypassing the need for auxiliary nonlinear components. To validate this approach, we formulate a five-currency arbitrage problem as a quadratic unconstrained binary optimization (QUBO) task and map it onto the Ising Hamiltonian. Numerical simulations, driven by experimentally calibrated modulation characteristics, demonstrate robust convergence to the ground state, successfully identifying the optimal arbitrage path with a profit rate of 1.0793. These results highlight the potential of heterogeneous PICs for realizing compact, stable, and scalable CIMs, paving a promising way toward high-performance photonic accelerators for financial modeling and broader combinatorial optimization.

Keywords: Ising machine, integrated photonics, heterogeneous integration, photonic integrated circuit

1. Introduction

Combinatorial optimization problems appear across numerous scientific and engineering fields, involving tasks such as resource allocation, scheduling, and path planning [1-3]. Solving these problems requires finding an optimal solution within an exponentially large search space. As problem size grows, the computational complexity rises sharply, making exact solutions increasingly impractical for conventional electronic computers, especially in large-scale and highly complex scenarios [4]. Recently, coherent Ising machines (CIMs) have emerged as an effective hardware approach for addressing combinatorial optimization challenges [5]. By mapping an optimization task onto the ground-state search of an Ising Hamiltonian implemented in an artificial spin network, CIMs leverage physical dynamics to efficiently approach optimal solutions [6, 7]. To enhance system stability and reduce physical footprint, optoelectronic oscillator (OEO)-based CIMs with self-feedback architectures have been introduced [8]. In these systems, the electro-optic modulator provides the

necessary nonlinearity, while iterative optoelectronic feedback drives the evolution of spin states toward the ground-state configuration.

In an OEO, nonlinearity is achieved by feeding the output of a laser diode into a Mach–Zehnder modulator (MZM) and detecting it with a photodiode. In current PICs, MZMs are predominantly implemented on silicon photonics platforms [9-12]. Silicon-based MZMs, whether relying on the carrier dispersion effect or the thermo-optic effect, offer full compatibility with CMOS processes but are limited by either restricted bandwidth or high power consumption [13-16]. In contrast, thin-film lithium niobate (TFLN) devices, benefiting from a strong electro-optic effect, exhibit significant potential for high-speed modulation. Nevertheless, a major challenge in TFLN platforms is the lack of integrated detection capabilities [17-21]. This motivates the integration of silicon photonics with TFLN to leverage the advantages of both platforms [22-25].

In this work, we therefore propose and demonstrate a heterogeneous photonic integrated circuit (PIC) for coherent Ising machines (CIMs). The proposed heterogeneous PIC integrates the ultra-low optical loss of silicon nitride (SiN) waveguides with lithium niobate (LN) modulator and germanium-silicon (Ge-Si) photodetector (PD), enabling high-bandwidth, low-insertion-loss, and highly linear optical modulation. By employing traveling-wave electrode designs, modulation bandwidths of several tens of gigahertz can be achieved, together with low driving voltages and excellent linearity. Thanks to the high thermal stability of SiN and the compatibility with CMOS fabrication processes, this heterogeneous approach offers a promising route for fully integrated CIMs aimed at solving combinatorial optimization problems.

2. Principle

Figure 1(a) illustrates the heterogeneous integrated device fabricated using standard foundry processes. The spot-size converters (SSCs), transmission waveguides, and multimode interferometers (MMIs) are implemented in SiN owing to its low coupling and propagation losses and excellent mode stability. The input wavelength of the laser is 1550nm. A silicon-based thermal-optic phase shifter (TOPS) is inserted between the SiN waveguide and the thin-film lithium niobate (TFLN). Silicon is selected for the TOPS because its thermo-optic coefficient is ~5× higher than that of LN, providing efficient phase tuning and temperature-drift compensation. MMI is used to split light into two paths. The TFLN Mach–Zehnder modulator (MZM) modulator serves as the device core, enabling ultra-high-speed modulation via the Pockels effect, while differential electrode driving supports broad modulation bandwidth. At the output, a Ge–Si photodetector (PD) monitors MZM output and interfaces with external circuits. Figure 1(b) presents the cross-sectional structure, comprising a multilayer heterogeneous waveguide: a bottom silicon layer for thermal phase tuning, a middle SiN layer for low-loss coupling and transmission, and a top LN layer for high-speed electro-optic modulation. The waveguide width is 2.3 μm; the LN and SiN thicknesses are 400 nm and 500 nm, respectively. The electrode height and spacing are 2 μm and 6.75 μm. Adiabatic tapers are employed to ensure smooth mode transitions and minimize insertion loss. In the SiN–Si transition, the SiN waveguide narrows while the Si waveguide widens, enabling efficient mode transfer through effective index matching. In the Si–LN transition, the Si waveguide tapers as the LN layer is introduced, guiding the optical mode into the LN ($n \approx 2.2$) electro-optic interaction region.

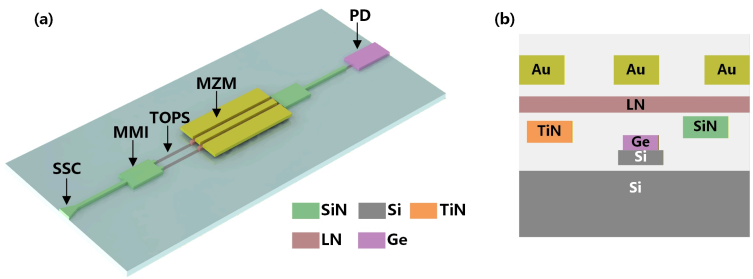

Figure 1. (a) Schematic and (b) cross section of the proposed heterogeneous CIM.

The modulation curve of MZM describes the relationship between the output optical voltage and the driving voltage, which is a cosine square nonlinear curve. In CIM based on opto-electronic feedback systems, the modulation curve of MZM is fitted to the nonlinearity shown in Equation [26], where k is the kth iteration, ξ is the Gaussian noise, the output optical voltage is mapped to the spin amplitude x_n, and the driving voltage is mapped to the feedback signal f_n. f_n is calculated from x_n and the coupling coefficient between spins J_{mn}, as shown in Equation , where α is the feedback strength and β is the coupling strength. The spin coupling matrix is constructed according to the specifically analyzed Ising problem. The evolution of the spin state can be realized through one iteration of the system. The Hamiltonian gradually decreases, and finally reaches the ground state. The optimal solution of the problem is obtained according to the spin of the ground state.

$$x_n[k+1] = cos^2\left(f_n[k] - \tfrac{\pi}{4} + \xi_n[k]\right) - \tfrac{1}{2} \quad (1)$$

$$f_n[k] = \alpha x_n[k] + \beta \sum_m J_{mn} x_m[k] \quad (2)$$

Here, we focus on the solving of currency arbitrage based on integrated CIM. Currency arbitrage aims to identify a closed exchange cycle among multiple currencies such that the final capital exceeds the initial investment, thereby yielding a theoretically risk-free return [27]. The optimal solution corresponds to the exchange path that maximizes the profit rate. This problem can be formulated as an optimal path search in a directed graph, where nodes represent currencies and weighted edges correspond to exchange rates. As such, currency arbitrage constitutes a typical combinatorial optimization problem, which can be naturally mapped into quadratic unconstrained binary optimization (QUBO) problem and efficiently solved using a CIM. We use a cost function to represent the earning rate of currency arbitrage as Equation , where b_{ik} is a binary variable, if the corresponding currency pair (currency i to currency k) is selected in the exchange path, $b_{ik} = 1$, otherwise $b_{ik} = 0$. And $\omega_{ik} = -\log r_{ik}$ is the negative logarithm of r_{ik} (the exchange rate of currency i and currency k). We take the negative logarithm of the exchange rate here to convert the total profit rate = $\Pi r_{ik} b_{ik}$ from quadrature to sum, in order to map it to the Ising model in the future.

$$C = \sum_{ik} \omega_{ik} b_{ik} \quad (3)$$

In addition, in order to avoid the illegal situation that the calculation results do not conform to the trading rules, we also introduced the penalty function of circular constraint as Equation .The first and second term forces the outflow and inflow of each node to be 1 or less. The third term forces the inflows and outflows of each node to be equal. The fourth term forbids traversing the same edge twice in different directions. Constraint violations increase the penalty function, with P = 0 if there are no violations. The total cost function (Ctot) is a linear combination of C and P, described by Equation , where A and B are positive coefficients, they can be used to adjust the proportion of cost function C and penalty function P in the total cost function. The values of these two parameters are crucial for finding the optimal solution. If the ratio of A to B is too large,

the proportion of penalty term P in the total cost term will be small, resulting in a situation where the Hamiltonian of the illegal solution is smaller than that of the legal solution. On the contrary, if the proportion of cost item C is small, the difference in Hamiltonian between different legal solutions is too small to distinguish, making it difficult to obtain the optimal solution. In practical simulations and experiments, we fix the value of A to 1 and adjust the value of B based on the weight ω_{ik} of each edge, so that B can satisfy the Hamiltonian of the illegal solution to be greater than that of the legal solution as small as possible.

$$P = \sum_i \sum_{k \neq k'} b_{ik} b_{ik'} + \sum_k \sum_{i \neq i'} b_{ik} b_{i'k} + \sum_i \left(\sum_k b_{ik} - \sum_k b_{ki} \right)^2 + \sum_{ik} b_{ik} b_{ki} \tag{4}$$

$$C_{tot} = A \bullet C + B \bullet P \tag{5}$$

The total energy (Hamiltonian, H) of an Ising model with the external magnetic fields is expressed as Equation , where σ_i (or σ_j) denotes the state of the i_{th} (or j_{th}) spin, J_{ij} is the coupling coefficient between the i_{th} and j_{th} spins, and h_i is the external magnetic field for the i_{th} spin.

$$H = -\sum_{ij} J_{ij} \sigma_i \sigma_j - \sum_i h_i \sigma_i \tag{6}$$

An n-currency arbitrage can be formulated as an Ising problem with external magnetic fields using n2 spins in a lattice. Since the binary variable b_{ik} in Equation has two indices (representing the i-th and k-th currencies respectively), we need to change the spin of one index in the original Hamiltonian expression to two, as Equation [28]. By equating Equation with Equation , we can solve the coupling matrix J_{ikjl} and external magnetic field hik of the Ising model of currency arbitrage. But first we have to convert the binary variable b_{ik} (= 0,1) to Ising spin σ_{ik} (= -1,1), as Equation . And J_{ikjl} and h_{ik} are shown in Equation and Equation , where □ is kronecker delta (equal to 1, otherwise 0).

$$H_c = -\sum_{i=1}^{n} \sum_{j=1}^{n} \sum_{k=1}^{n} \sum_{l=1}^{n} J_{ikjl} \sigma_{ik} \sigma_{jl} - \sum_{i=1}^{n} \sum_{k=1}^{n} h_{ik} \sigma_{ik} \tag{7}$$

$$b_{ik} = \frac{\sigma_{ik}+1}{2} \tag{8}$$

$$J_{ikjl} = -\frac{B}{4} \left(2\delta_{ij} + 2\delta_{kl} - 2\delta_{ij}\delta_{kl} - \delta_{il} - \delta_{kj} + \delta_{kj}\delta_{il} \right) \tag{9}$$

$$h_{ik} = -\frac{A}{2} \omega_{ik} - B\left(n - \frac{1}{2}\right) \tag{10}$$

Due to the existence of external magnetic field h_{ik}, our CIM is not suitable for dealing with such problems. To eliminate h_{ik}, a redundant spin with the state σ(n+1)(n+1) fixed to "+ 1" is introduced to as Equation [29], where new coupling matrix $J`_{ikjl}$ as shown in Equation .

$$\begin{aligned} H_c = &-\sum_{i=1}^{n} \sum_{k=1}^{n} \sum_{j=1}^{n} \sum_{l=1}^{n} J_{ikjl} \sigma_{ik} \sigma_{jl} - \sum_{i=1}^{n} \sum_{k=1}^{n} h_{ik} \sigma_{ik} \sigma_{(n+1)(n+1)} = \\ &-\sum_{i=1}^{n+1} \sum_{k=1}^{n+1} \sum_{j=1}^{n+1} \sum_{l=1}^{n+1} J'_{ikjl} \sigma_{ik} \sigma_{jl} \end{aligned} \tag{11}$$

$$J'_{ikjl} = \begin{cases} J_{ikjl} & i,k,j,l \in (1,2,\ldots,n) \\ \frac{h_{ik}}{2} & i,k \in (1,2,\ldots,n) \quad and \quad j = l = n+1 \\ \frac{h_{jl}}{2} & j,l \in (1,2,\ldots,n) \quad and \quad i = k = n+1 \\ 0 & otherwise \end{cases} \tag{12}$$

3. Results

Figure 2 presents the measured characteristics of the proposed heterogeneous integrated modulator. Figure 2(a) shows the optical output voltage as a function of the input driving voltage, obtained through photodetector conversion. The input voltage ranges from –60 to 40 V, and the optical response exhibits a trigonometric-like

behavior with two distinct effective periods. Within –60 to 0 V, the modulator's half-wave voltage is approximately 40 V, while within 0 to 40 V, it decreases to about 30 V, reflecting the asymmetry in the modulation response.

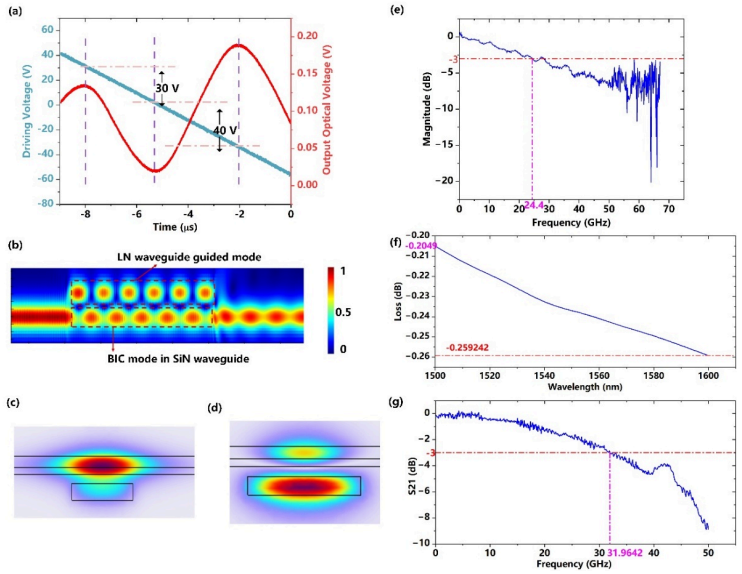

Figure 2. (a) Measured relationship between input driving voltage and output optical voltage of the heterogeneous integrated modulator. (b) Optical field distribution at the junction of LN and SiN. Optical field distributions in (c) LN and (d) SiN layers. (e) PD bandwidth measurement. (f) Interlayer coupling loss measurement. (g) Modulator bandwidth measurement

The main reason for the low modulation efficiency is that the electrode spacing we designed is 6.75 μm. If we reduce the electrode spacing and design the MZM structure, the modulation efficiency can be further improved. Figure 2(b) illustrates the light field distribution at the LN and SiN interface. The field forms a hybrid mode resembling quasi-bound states in the continuum, simultaneously occupying both the SiN and LN layers. The absence of abrupt mode transitions ensures low optical loss at the junction between the SiN waveguide and the hybrid LN–SiN region.

This low loss characteristic is experimentally verified in Figure 2(f), which shows that the interlayer coupling loss remains between 0.2 and 0.26 dB across a broad wavelength range of 1500 to 1600 nm. Figure 2(e) presents the frequency response of the photodetector, indicating a 3 dB bandwidth of 24.4 GHz. Figure 2(g) displays the modulator response, with a measured 3 dB bandwidth of approximately 32 GHz, demonstrating the device capability for high speed signal processing.

Based on the data in Figure 2(a), we perform a nonlinear fitting of the CIM and conduct a simulation study of a five-currency arbitrage problem involving CNY, USD, EUR, JPY, and GBP. The exchange rates used are shown in Table 1 and were obtained from publicly available sources. The optimal arbitrage path is CNY → GBP → JPY → CNY, yielding a profit rate of 0.1098 × 196.6 × 0.05 = 1.0793 (Calculate again by exhaustive method). To provide a more intuitive representation, a directed graph is used to illustrate all possible exchange paths among the five currencies, as shown in Figure 3, with the optimal arbitrage path highlighted in red.

Table 1. The exchange rates of 5 currencies

	CNY	USD	EUR	JPY	GBP
CNY	1	0.1401	0.1171	19.99	0.1098
USD	7.1362	1	0.8676	146.0	0.7437
EUR	8.2290	1.1529	1	168.5	0.8570
JPY	0.0500	0.006849	0.005937	1	0.005086
GBP	9.5860	1.3440	1.1664	196.6	1

Based on the profit rate, the total cost function is formulated as shown in Equation (4) and then mapped to the Hamiltonian representation to calculate the spin coupling matrix, as given in Equation (11). Python is used to simulate the CIM (we use the experimentally measured static MZM transfer curve to model the nonlinearity) and determine the optimal exchange path, with the results presented in Figure 4.

The five currencies (CNY, USD, EUR, JPY, GBP) are numbered sequentially, and 25 spins are used to represent whether each currency pair is included in the exchange path. For instance, a positive value of σ_{15} indicates that the exchange from currency 1 (CNY) to currency 5 (GBP) is selected. During the simulation, all 25 spin states evolve iteratively. In the final configuration, three spins are positive while the remaining spins are negative. Figure 4(a) also shows a spin with a positive value that does not correspond to a currency pair; this redundant spin, introduced as described in Equation (10), serves to eliminate the external magnetic field term in the Hamiltonian and has no physical representation in the exchange path. The three positive spins, σ_{15}, σ_{54}, and σ_{41}, correspond to the exchange path CNY → GBP → JPY → CNY, which is the optimal arbitrage path with a maximum profit rate of 1.0793.

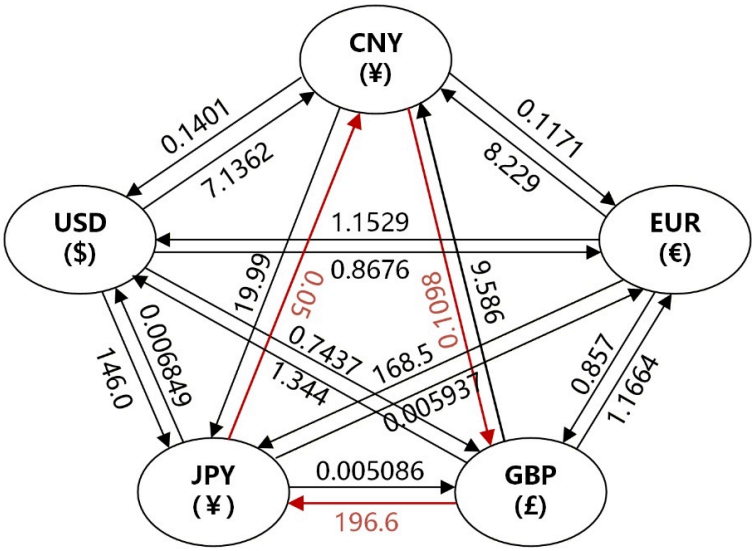

Figure 3. A directed graph showing all currency exchange paths, the optimal arbitrage path (CNY -> GBP -> JPY -> CNY) is highlighted in red

To evaluate the performance of the CIM, 2000 independent simulations were conducted and the results of each run were recorded, as shown in Figures 4(c) and 4(d). The data indicate that the success rate of finding the optimal solution increases with the number of iterations, reaching 0.017 after 2000 simulations.

Suboptimal solutions were also analyzed, revealing that the success rates for achieving profit margins exceeding 1.04 and 1.06 are 0.1395 and 0.0555, respectively.

The success rate of our simulation is not very high. There are two main reasons for our analysis. Firstly, the currency arbitrage problem is a relatively complex issue. For an arbitrage problem involving n currencies, the possible paths include 2, 3...n currencies, forming a factorial relationship with the number of currencies. With a large number of total trading paths, the probability of obtaining an optimal solution is relatively low. Secondly, in the mathematical expression of the currency arbitrage problem, there are two terms: the cost term and the penalty term. These two terms actually have a game-theoretic relationship. If the weight of the cost term is increased, the energy gap between the optimal solution and the suboptimal solution will increase, and the probability of the optimal solution among legal solutions will rise. However, the proportion of the penalty term decreases, which in turn reduces the probability of legal solutions. Ultimately, the probability of the optimal solution does not increase significantly. Conversely, the probability of legal solutions increases, but the probability of the optimal solution among legal solutions decreases.

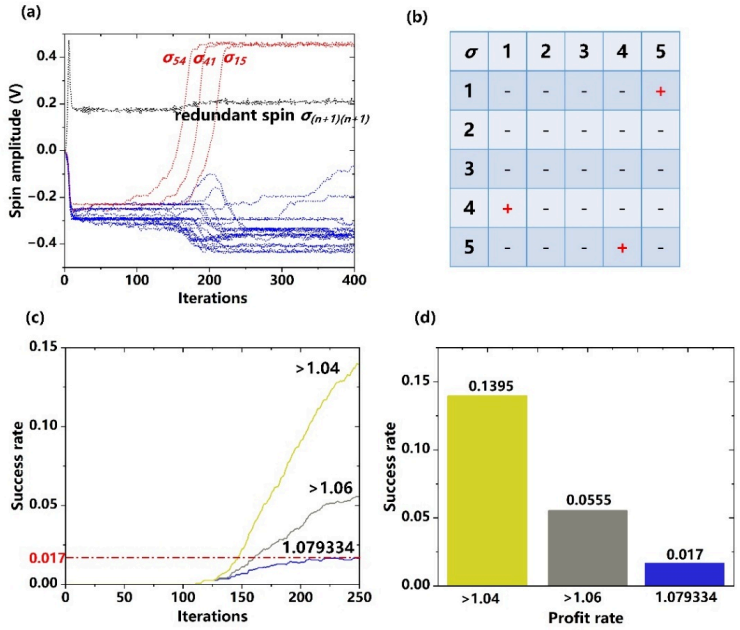

σ	1	2	3	4	5
1	-	-	-	-	+
2	-	-	-	-	-
3	-	-	-	-	-
4	+	-	-	-	-
5	-	-	-	+	-

Figure 4. (a) Evolution of spin amplitude with iteration (calculated from equation 1). (b) Spin state of ground state. (c) Evolution of success rate with iteration. (d) The success rate of profit rate >1.04, 1.06 and 1.079334 (the best)

In Figure 4 (c), we mainly consider the saturation feature of the success rate of the optimal solution. After about 250 iterations, the optimal solution can reach saturation, and there are still two suboptimal solutions. To achieve saturation of suboptimal solutions, the number of iterations should be increased. However, according to our simulation results, the success rate of the optimal solution began to decline after approximately 300 iterations, so we ultimately only considered 250 iterations. In this work, the matrix vector multiplication is performed based on algorithm, and it can be further realized based on optical structure, such as MZI grid with either Reck [30] or Clements [31] structures.

4. Conclusions

In conclusion, we have demonstrated an opto-electronic CIM based on a heterogeneous PIC that monolithically integrates a SiN–LN electro-optic modulator, a silicon-based thermal phase shifter, and a Ge-Si PD. This multi-material integration leverages the ultra-low optical loss of SiN waveguides, the high-speed response of LN, the efficient and stable thermal tunability of silicon, and the high-responsivity of Ge-Si PD, providing a compact and robust hardware platform for CIM. By directly incorporating the experimentally measured nonlinear modulation transfer function of the SiN–LN modulator into an opto-electronic feedback loop, Ising spin dynamics are implemented without the need for additional nonlinear elements. As a proof of concept, the system successfully solves a five-currency arbitrage problem, reliably identifying the optimal exchange cycle that maximizes profit. These results highlight the feasibility and advantages of heterogeneous PICs for achieving stable, scalable, and high-performance CIM, offering a promising pathway toward large-scale photonic optimization processors for financial applications and other complex combinatorial problems.

Authorship

C.Z. and Y.X. contributed equally to this work. Conceptualization, C.Z.; methodology, Y.X.; validation, C.Z., Y.X. and Z.Z.; investigation, C.Z., Y.X. and Z.Z.; writing—original draft preparation, Y.X.; writing—review and editing, C.Z., Y.X., Z.Z.; visualization, C.Z., Y.X. and Z.Z.; supervision, G.C.

Funding project

This work was supported by the National Key Research and Development Program of China (2024YFB2808600); National Natural Science Foundation of China (62405035, W2521113); Natural Science Foundation of Chongqing Municipality (CSTB2025NSCQ-GPX0737, CX2025019).

References

[1] Vygen, B.K.J. Combinatorial Optimization. Springer 2011.

[2] Gao, Y.; Chen, G.; Qi, L.; Fu, W.; Yuan, Z.; Danner, A.J. Photonic Ising machines for combinatorial optimization problems. *Applied Physics Reviews 2024, 11*, doi: 10.1063/5.0216656.

[3] Ishibashi, S.; Arai, M.; Li, A.; Takesue, H.; Inaba, K.; Aihara, K.; Hasegawa, M. *High-Speed Resource Allocation for Multi-User NOMA Systems Using a Coherent Ising Machine. 2025*, 231-235, doi: 10.1109/icoin63865.2025.10992949.

[4] Lan, Y.; Chen, G.; Gao, Y.; Fu, W.; Danner, A.J. An Integrated All-Optical Ising Machine with Unlimited Spin Array Size and Coupling. *Advanced Photonics Research 2024, 5*, 2400004, doi: 10.1002/adpr.202400004.

[5] Mohseni, N.; McMahon, P.L.; Byrnes, T. Ising machines as hardware solvers of combinatorial optimization problems. *Nature Reviews Physics 2022, 4*, 363-379, doi: 10.1038/s42254-022-00440-8.

[6] Lucas, A. Ising formulations of many NP problems. *Frontiers in Physics 2014*, Volume 2 - 2014, doi: 10.3389/fphy.2014.00005.

[7] Yang, S.; Shin, J.; Kim, T.; Moon, K.-W.; Kim, J.; Jang, G.; Hyeon, D.S.; Yang, J.; Hwang, C.; Jeong, Y.; et al. Integrated neuromorphic computing networks by artificial spin synapses and spin neurons. *NPG Asia Materials 2021, 13*, 11, doi: 10.1038/s41427-021-00282-3.

[8] Böhm, F.; Verschaffelt, G.; Van der Sande, G. A poor man's coherent Ising machine based on opto-electronic feedback systems for solving optimization problems. *Nature Communications 2019, 10,* 3538, doi: 10.1038/s41467-019-11484-3.

[9] Li, Z.; Gan, R.; Chen, Z.; Deng, Z.; Gao, R.; Chen, K.; Guo, C.; Zhang, Y.; Liu, L.; Yu, S.; et al. Scalable On-Chip Optoelectronic Ising Machine Utilizing Thin-Film Lithium Niobate Photonics. *ACS Photonics 2024, 11*, 1703-1714, doi: 10.1021/acsphotonics.4c00003.

[10] Al-Kayed, N.; St-Arnault, C.; Morison, H.; Aadhi, A.; Huang, C.; Tait, A.N.; Plant, D.V.; Shastri, B.J. Programmable 200 GOPS Hopfield-inspired photonic Ising machine. *Nature 2025, 648*, 576-584, doi: 10.1038/s41586-025-09838-7.

[11] Zhang, Z.; Chen, G.; Gao, Y.; Fu, W.; Lim, S.T.; Prabhakar, A.; Danner, A.J.; Zhu, T. Integrated optoelectronic Ising machine based on silicon photonics. *In Proceedings of the 2025 Optical Fiber Communications Conference and Exhibition (OFC), 30* March-3 April 2025, 2025; pp. 1-3.

[12] Chen, Z.; Liu, M.; Cheng, S.; Wang, J.; Yi, Y.; Li, B.; Tang, C.; Gao, F. Bilayer graphene metasurface with dynamically reconfigurable terahertz perfect absorption. *Current Applied Physics 2025, 80*, 282-290, doi: 10.1016/j.cap.2025.10.001.

[13] Fang, S.; Fan, J.; Zhang, Q.; Jiang, X.; Wei, Z.; Yang, J.; Yu, H. Optimal linear operation point control of silicon-based Mach-Zehnder modulator. Opt. *Express 2025, 33*, 33609-33619, doi: 10.1364/OE.563164.

[14] Wang, H.; Tan, J.Y.S.; Tang, H.; Teo, T.Y.; Xie, W.; Leong, C.P.; Gu, W.; Li, C.; Lo, P.G.-Q. 90 GHz Silicon Mach-Zehnder Modulator with Integrated Equalizer for 1.6 Tbps (200G/λ) IMDD Transceivers. *In Proceedings of the Optical Fiber Communication Conference (OFC) 2025*, San Francisco, California, 2025/03/30, 2025; p. M2K.1.

[15] Li, J.; Li, X.; Luo, M.; Zhang, X.; Yang, C.; Zhang, H.; Fan, R.; Wang, Q.; Wang, D.; Cai, X.; et al. Demonstration of 200 Gb/s/λ PON in O-Band With High-Bandwidth TFLN Modulator. *Journal of Lightwave Technology 2023, 41*, 3594-3602, doi: 10.1109/JLT.2023.3256361.

[16] Chen, G.; Yu, Y.; Shi, Y.; Li, N.; Luo, W.; Cao, L.; Danner, A.J.; Liu, A.-Q.; Zhang, X. High-Speed Photodetectors on Silicon Photonics Platform for Optical Interconnect. *Laser & Photonics Reviews 2022, 16,* 2200117, doi: 10.1002/lpor.202200117.

[17] Chen, G.; Gao, Y.; Lin, H.-L.; Danner, A.J. Compact and Efficient Thin-Film Lithium Niobate Modulators. *Advanced Photonics Research 2023, 4*, 2300229, doi: 10.1002/adpr.202300229.

[18] Qin, Y.-Y.; Gu, X.-W.; Tang, J.; Ye, H.-Y.; Dong, W.-H.; Song, Y.-J.; Qian, G.; Zhang, X.-Y.; Zhang, T. Broadband, high-linearity TFLN electro-optic modulator for integrated microwave photonics using reconfigurable dual-parallel modulation. Opt. *Express 2025, 33*, 13805-13815, doi: 10.1364/OE.554821.

[19] Tan, Y.; Niu, S.; Billet, M.; Singh, N.; Niels, M.; Vanackere, T.; Van Kerrebrouck, J.; Roelkens, G.; Kuyken, B.; Van Thourhout, D. Micro-transfer Printed Thin Film Lithium Niobate (TFLN)-on-Silicon Ring Modulator. *ACS Photonics 2024, 11*, 1920-1927, doi: 10.1021/acsphotonics.3c01869.

[20] Chen, G.; Li, N.; Ng, J.D.; Lin, H.-L.; Zhou, Y.; Fu, Y.H.; Lee, L.Y.T.; Yu, Y.; Liu, A.-Q.; Danner, A.J. Advances in lithium niobate photonics: development status and perspectives. *Advanced Photonics 2022, 4*, 034003, doi: 10.1117/1.Ap.4.3.034003.

[21] Wu, P.; Zhao, W.; Cui, L.; Jiang, P. High absorption broadband solar energy device and thermal emitter based on titanium metamaterials. *International Journal of Thermal Sciences 2026, 223*, 110620, doi: 10.1016/j.ijthermalsci.2025.110620.

[22] Vanackere, T.; Vandekerckhove, T.; Bogaert, L.; Billet, M.; Poelman, S.; Cuyvers, S.; Van Kerrebrouck, J.; Moerman, A.; Caytan, O.; Singh, N.; et al. Heterogeneous integration of a high-speed lithium niobate modulator on silicon nitride using micro-transfer printing. *APL Photonics 2023, 8,* doi: 10.1063/5.0150878.

[23] Valdez, F.; Mere, V.; Mookherjea, S. 100& #x2009; & #x2009; GHz bandwidth, 1 volt integrated electro-optic Mach& #x2013; Zehnder modulator at near-IR wavelengths. *Optica 2023, 10*, 578-584, doi: 10.1364/OPTICA.484549.

[24] Li, Z.; Chen, Y.; Zhang, J.; Xu, F.; Wang, S.; Ou, X.; Cai, Y.; Yu, M. Hybrid Silicon Nitride/Lithium Niobate Electro-Optical Modulator with Wide Optical Bandwidth and High RF Bandwidth Based on Ion-cut Wafer-

level Bonding Technology. *In Proceedings of the Optical Fiber Communication Conference (OFC) 2025*, San Francisco, California, 2025/03/30, 2025; p. Th1E.1.

[25] Jin, Z.; Liu, M.; Cheng, S.; Yi, Z.; Wang, J.; Li, B. Broadband tunable metasurface absorbing device in the terahertz band based on single-layer graphene. *Modern Physics Letters B 2025, 40*, 2650017, doi: 10.1142/S021798492650017X.

[26] Hart, J.D.; Schmadel, D.C.; Murphy, T.E.; Roy, R. Experiments with arbitrary networks in time-multiplexed delay systems. *Chaos: An Interdisciplinary Journal of Nonlinear Science 2017, 27*, doi: 10.1063/1.5016047.

[27] Tatsumura, K.; Hidaka, R.; Yamasaki, M.; Sakai, Y.; Goto, H. A Currency Arbitrage Machine Based on the Simulated Bifurcation Algorithm for Ultrafast Detection of Optimal Opportunity. *In Proceedings of the 2020 IEEE International Symposium on Circuits and Systems (ISCAS)*, 12-14 Oct 2020, 2020; pp. 1-5.

[28] Dan, A.; Shimizu, R.; Nishikawa, T.; Bian, S.; Sato, T. Clustering Approach for Solving Traveling Salesman Problems via Ising Model Based Solver. *In Proceedings of the 2020 57th ACM/IEEE Design Automation Conference (DAC)*, 20-24 July 2020, 2020; pp. 1-6.

[29] Zhang, T.; Han, J. Efficient Traveling Salesman Problem Solvers using the Ising Model with Simulated Bifurcation. *In Proceedings of the 2022 Design, Automation & Test in Europe Conference & Exhibition (DATE),* 14-23 March 2022, 2022; pp. 548-551.

[30] Reck, M.; Zeilinger, A.; Bernstein, H.J.; Bertani, P. Experimental realization of any discrete unitary operator. *Physical Review Letters 1994, 73*, 58-61, doi: 10.1103/PhysRevLett.73.58.

[31] Clements, W.R.; Humphreys, P.C.; Metcalf, B.J.; Kolthammer, W.S.; Walmsley, I.A. Optimal design for universal multiport interferometers. *Optica 2016, 3*, 1460-1465, doi: 10.1364/OPTICA.3.001460.